Soroush Heidari Pahlavian
Conquer Chiari Research Center,
Department of Mechanical Engineering,
The University of Akron,
Akron, OH 44325
e-mail: sh113@uakron.edu

Alexander C. Bunck
Department of Radiology,
University Hospital of Cologne,
Cologne 50923, Germany
e-mail: alexander.bunck@uk-koeln.de

Francis Loth
Conquer Chiari Research Center,
Department of Mechanical Engineering,
The University of Akron,
Akron, OH 44325
e-mail: loth@uakron.edu

R. Shane Tubbs
Children's of Alabama,
Birmingham AL 35233;
Department of Anatomical Sciences,
St. George's University,
St. George, Grenada;
Centre for Anatomy and Human Identification,
Dundee University,
Dundee DD1 4HN, UK
e-mail: Shane.Tubbs@childrensal.org

Theresia Yiallourou
Laboratory of Hemodynamics and
Cardiovascular Technology,
EPFL,
Lausanne 1015, Switzerland
e-mail: thiresia.giallourou@epfl.ch

Jan Robert Kroeger
Department of Radiology,
University Hospital of Cologne,
Cologne 50923, Germany
e-mail: janrobertkroeger@gmail.com

Walter Heindel
Department of Clinical Radiology,
University Hospital of Muenster,
Muenster 48149, Germany
e-mail: heindel@uni-muenster.de

Bryn A. Martin
Conquer Chiari Research Center,
Department of Mechanical Engineering,
The University of Akron,
Akron, OH 44325
e-mail: director@chiari-research.org

Characterization of the Discrepancies Between Four-Dimensional Phase-Contrast Magnetic Resonance Imaging and In-Silico Simulations of Cerebrospinal Fluid Dynamics

The purpose of the present study was to compare subject-specific magnetic resonance imaging (MRI)-based computational fluid dynamics (CFD) simulations with time-resolved three-directional (3D) velocity-encoded phase-contrast MRI (4D PCMRI) measurements of the cerebrospinal fluid (CSF) velocity field in the cervical spinal subarachnoid space (SSS). Three-dimensional models of the cervical SSS were constructed based on MRI image segmentation and anatomical measurements for a healthy subject and patient with Chiari I malformation. CFD was used to simulate the CSF motion and compared to the 4D PCMRI measurements. Four-dimensional PCMRI measurements had much greater CSF velocities compared to CFD simulations (1.4 to 5.6× greater). Four-dimensional PCMRI and CFD both showed anterior and anterolateral dominance of CSF velocities, although this flow feature was more pronounced in 4D PCMRI measurements compared to CFD. CSF flow jets were present near the nerve rootlets and denticulate ligaments (NRDL) in the CFD simulation. Flow jets were visible in the 4D PCMRI measurements, although they were not clearly attributable to nerve rootlets. Inclusion of spinal cord NRDL in the cervical SSS does not fully explain the differences between velocities obtained from 4D PCMRI measurements and CFD simulations.
[DOI: 10.1115/1.4029699]

Keywords: cerebrospinal fluid, computational fluid dynamics, 4D phase-contrast MRI, type 1 chiari malformation, hydrocephalus, spinal cord nerve root, denticulate ligament, spinal subarachnoid space, intrathecal drug delivery

Introduction

CSF dynamics are thought to play an important role in central nervous system (CNS) physiology. The investigation of CSF dynamics in the SSS could help to gain a deeper understanding of its normal function and significance in the development of CNS pathophysiologies such as type 1 Chiari malformation (CMI) [1], syringomyelia [2,3], and hydrocephalus [4] and application to intrathecal drug delivery [5,6].

For the last few decades, single-slice 2D phase-contrast MR flow imaging (2D PCMRI) has been the main in vivo approach to study CSF dynamics in research and clinical routine [7–10]. Usage of 2D PCMRI provides one component of velocity for a given slice. To obtain all three components of velocity, two additional scans are required, adding imaging time. Many additional

Manuscript received August 18, 2014; final manuscript received January 21, 2015; published online February 20, 2015. Assoc. Editor: Tim David.

2D PCMR image slices would be needed to map a 3D velocity field within a region of interest (e.g., the complex 3D vortex patterns that may be present in the cervical spine in CMI patients [8]). Application of 2D PCMRI for this purpose would require an impractical amount of imaging time. Time-resolved 3D phase-contrast MRI (4D PCMRI) has been increasingly appreciated as a rapid and novel approach to investigate complex CSF flow phenomena [11–15] by quantification of three-directional velocity information within a volume of interest [16].

CFD has been applied in models with varying degrees of anatomical complexity to help understand the underlying physiology of CSF flow [17–19]. A review of CSF flow studies using CFD was published by Shaffer et al. [20] and Yiallourou et al. [21]. A subject-specific CFD model of the cervical SSS CSF flow was developed by our research group with idealized spinal cord NRDL [19]. This study showed that NRDL has an important impact on CSF dynamics in terms of velocity field and flow patterns. Another study by our research group found that subject-specific CFD simulation of CSF flow in the cervical spine resulted in 3.4 to 8.4× smaller peak CSF velocities than in vivo 4D PCMRI measurements [21]. This study provided impetus for a rigorous analysis of the various reasons that might underpin the differences in CSF flow quantified by CFD simulation and in vivo PCMRI measurements.

The goal of the present variational analysis study was to determine if addition of NRDL in the CFD modeling approach resulted in better agreement with the in vivo 4D PCMRI measurements. In order to account for hydrodynamic complexities present in a disease state, CFD simulations and in vivo measurements were performed on a healthy subject and a CMI patient. For each case, we compared various features of CSF motion in CFD simulations and 4D PCMRI measurements.

Materials and Methods

Patients and Subjects. This study was approved by the institutional review board. Written informed consent was obtained prior to completion of the MRI exams. MRI data were anonymized prior to postprocessing.

MRI Geometry and 4D PCMRI CSF Flow Measurements. MRI data acquisition was performed as previously described [19]. In brief, MRI measurements were acquired on a 1.5-Tesla MRI (Achieva 2.6, Philips, Best, The Netherlands) with a standard 16-channel head and neck coil. A retrospective electrocardiogram-triggered, T1-weighted, segmented gradient echo sequence (T1-TFE) with isotropic 1.5 mm voxel size was used for the 4D PCMRI measurements. The 3D field of view was adjusted to cover the craniocervical junction and the entire cervical thecal sac, laterally and extending beyond the inner confinement of the foramen magnum (FC). Encoding velocity was set to 10 and 20 cm/s for the healthy and patient case, respectively. The cardiac cycle was encoded in 13 and ten phases for the healthy and patient cases, respectively, with a heart rate of 76.9 and 125 beats per minute (total 4D PCMRI imaging time was 8–14 min) [12]. To obtain anatomic data for geometric reconstruction of the spinal cord and dura, a T2-weighted 3D turbo spin-echo (TSE) imaging sequence was acquired with 0.8 mm isotropic resolution covering the craniocervical junction and the entire cervical thecal sac. Acquisition time for the TSE imaging was 3–5 min depending on the field of view. Subjects were advised to remain still during scanning, and no other precautions were used to prevent movement.

Subject-Specific Anatomical Geometries With Addition of Idealized NRDL. We used subject-specific healthy and CMI anatomical geometries that have been previously reported (a 22-year-old/male healthy volunteer, HVb, and a 5-year-old/male CMI patient with mild tonsillar descend below the FM, CM4 in Yiallourou et al.) [21]. ITK SNAP (version 2.2, PA) was used for the manual segmentation to reconstruct the three-dimensional anatomy of the cervical SSS, containing the dura mater and spinal cord, from the T2-weighted MRI images. Geometries were segmented several centimeters beyond the cervical region superiorly and inferiorly to avoid issues caused by short entry length or backflow at the models outlet. The resulting surface models were then smoothed and idealized NRDL were designed and added using AUTODESK MAYA (version 2012, Autodesk Inc., Mill Valley, CA) to form a composite anatomical model of the cervical SSS (Fig. 1). Size and placement of NRDL within the spinal canal were obtained from anatomical data found in literature [22–24] and visual inspection of the high-resolution MRI images (average thickness of nerve rootlets and denticulate ligaments were 1.4 and 0.1 mm, respectively). More details about this process is described by Pahlavian et al. [19].

CFD Simulations. CFD simulations were carried out based on the methodology and setup described previously [19]. In brief, a nonuniform unstructured rigid-walled computational mesh was

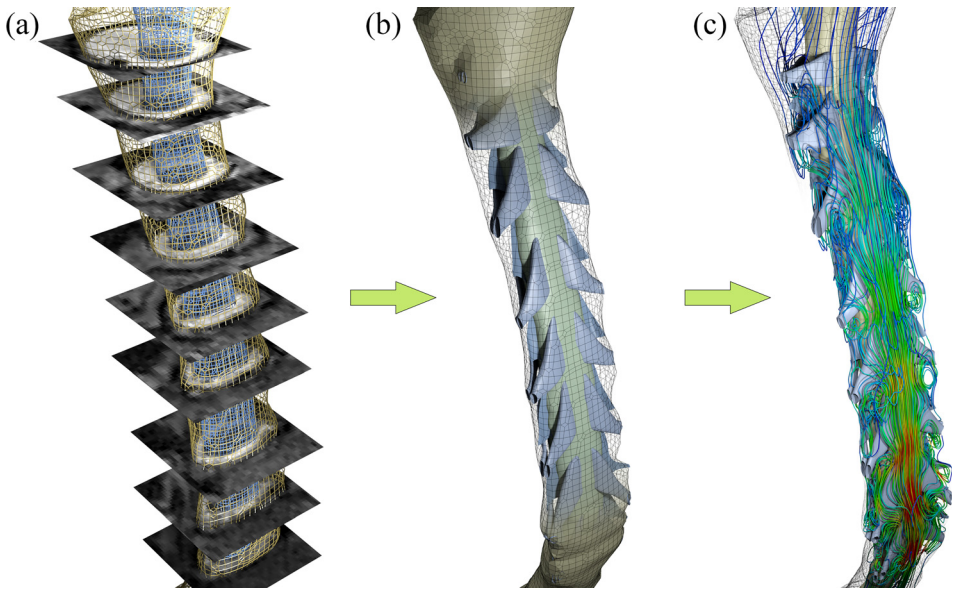

Fig. 1 Modeling process for the cervical SSS in the healthy case. (*a*) MR image segmentation to reconstruct the SSS. (*b*) Addition of idealized NRDL. (*c*) CSF flow simulation using CFD.

generated for the healthy and patient geometry using ANSYS ICEM CFD (version 14.0, ANSYS Inc., Canonsburg, PA). ANSYS FLUENT (version 14.0, ANSYS Inc., Canonsburg, PA) was used to carry out the CFD simulations. CSF was considered to be an incompressible Newtonian fluid with the same rheological properties as water at body temperature [25] and its flow was assumed to be laminar. This assumption was confirmed after calculation of the Reynolds number, based on the internal flow for each case, which did not exceed 350. The anatomical boundaries were considered to be rigid. Uniform velocity inlet and zero pressure outlet boundary conditions were imposed at the caudal and cranial end of the models, respectively.

Cross sections of the CSF flow domain for the 4D PCMRI measurements were manually segmented at nine axial slices below the FM to the first thoracic vertebrae. The CSF flow waveform was computed at each axial slice by integration of the velocity over the cross section (Fig. 2). The CSF flow waveform at each axial location was offset to obtain the zero net CSF flow per cycle. The offset values for the two cases were smaller than 0.2 cm^3/s. The CSF flow waveform was found to vary along the spine for the healthy subject and CMI patient. For each case, the CSF flow waveform with the greatest amplitude was selected as the unsteady velocity inlet boundary condition for the CFD simulations (C3 for the healthy case and C2M for the CMI patient, Fig. 2). The rational for selection of the waveforms with greatest amplitude was because a previous study by our group [21] showed peak velocities from subject-specific CFD simulations to be 3.4 to 8.4× smaller than 4D PCMRI measurements. Thus, the CSF waveforms with the greatest amplitude were selected to minimize any underprediction of CSF velocities in the CFD simulations.

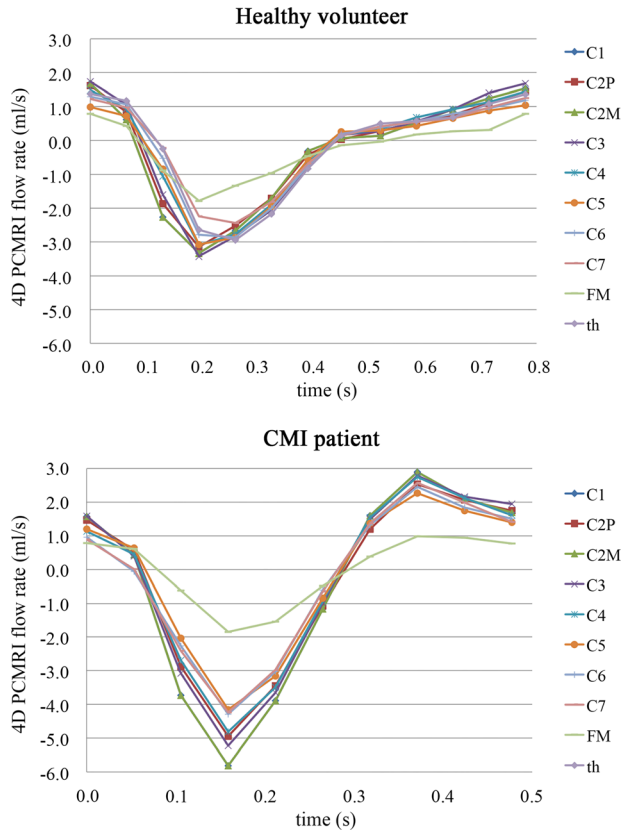

Fig. 2 In vivo CSF flow waveforms measured by 4D PCMRI for the healthy subject (top) and CMI patient (bottom) along the spine from C1 to the 1st thoracic vertebrae (th). Note, the magnitude of CSF flow amplitude changes along the cervical spine; a change likely due to SSS compliance. For the present study, the waveform with the greatest amplitude was used as the CFD flow boundary condition. This waveform was located at C3 for the healthy volunteer and at C2M for the CMI patient (C2P = C2 spinous process, C2M = middle of C2 vertebrae).

Assessment of CFD and 4D PCMRI Data. The spatial velocity patterns obtained from CFD were visualized and analyzed in the healthy and CMI models using ENSIGHT (version 10.0, CEI Inc., Apex, NC). The maximum value of through-plane velocities was determined within the nine axial cross sections (FM to C7, Fig. 1) at two time points; peak CSF flow in the caudal (systole, negative directed flow) and cranial (diastole, positive directed flow), directions. Through-plane velocities at each axial plane were calculated as the components of velocity vectors in the direction orthogonal to that plane. The average values of the peak systolic velocities (APV_S) and peak diastolic velocities (APV_D) were quantified over the nine axial cross sections.

Four-dimensional PCMRI measurements were visualized using the GTFLOW software (version 1.6.4, Gyrotools Ltd., Zurich, Switzerland). The flow was quantified at each of the nine axial planes analysed by CFD located from the FM to C7. The regions of interest (ROIs) excluded regions with blood flow through the vertebral and intra and epidural vessels by assessing direction of flow over time when using the PC images as described by Yiallourou et al. [21].

Results

Through-plane peak systolic and diastolic velocities measured by 4D PCMRI were 1.4 to 5.6× greater in magnitude than those computed by CFD (Fig. 3). For the healthy volunteer, the 4D PCMRI and CFD values of APV_S/APV_D were $-6.0 \pm 1.7/3.4 \pm 0.7$ and $-3.3 \pm 1.3/2.0 \pm 0.8$ cm/s, respectively. For the CMI patient, the 4D PCMRI and CFD values of APV_S/APV_D were $-12.2 \pm 4.2/7.2 \pm 2.2$ and $-4.4 \pm 0.4/3.3 \pm 0.4$ cm/s, respectively. Differences between the CFD and 4D PCMRI velocities were greatest in the caudal direction (systolic) at the C5 and C1 level in the healthy volunteer and CMI patient, respectively,

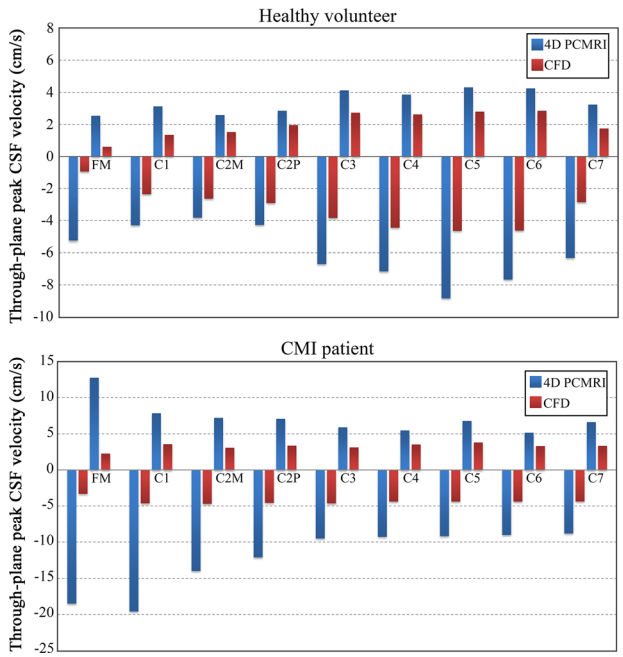

Fig. 3 Comparison of peak systolic (negative values) and peak diastolic (positive values) CSF velocities along the cervical spine between 4D PCMRI and CFD for the healthy volunteer (top) and CMI patient (bottom). Peak systolic and peak diastolic velocities were defined as the maximum magnitude of through-plane velocities that occurred anywhere within the designated cross sections at the time points corresponding to peak systole and peak diastole, respectively.

(Fig. 3). Four-dimensional PCMRI showed greater spatial velocity variation along the cervical SSS than CFD (Fig. 3).

Greater velocities at the axial measurement planes were observed in 4D PCMRI results compared to CFD results (Fig. 4). Also, spatial variation of velocities within the planes was more evident in the 4D PCMRI measurements than in the CFD. In the healthy case, the difference in velocity magnitude and distribution was more noticeable at planes with greater distance from the cranium. In contrast, the difference between the CFD and 4D PCMRI velocity field was greater at planes near the FM for the patient case, with unilateral high-velocity jets in these planes detected only in the 4D PCMRI images.

Despite the differences mentioned above, some similarities were observed between velocity distribution patterns obtained from CFD and 4D PCMRI. Greater CSF velocities were observed by 4D PCMRI for both subjects in the anterior and anterolateral regions of the SSS. The anterior and anterolateral dominance of CSF flow was seen in CFD results at some of the planes for both cases (C1, C4, C5, C6, and C7 in healthy case and FM, C1, C3, and C5 in patient case). Anterior dominance of flow was less pronounced in the CFD results in comparison to the 4D PCMRI results. Unlike the 4D PCMRI results, posterior velocity magnitudes obtained from CFD were comparable or even greater than anterior velocities at some planes. The posterior dominance of CFD velocities at the C5/C6 region is shown in the midsagittal velocity profiles in Fig. 5 (also see Animation#1 and Animation#2 in supplementary materials (Supplemental videos are available under the "Supplemental Data" tab for this paper on the ASME Digital Collection)). In addition, relatively high and concentrated regions (jets) of CSF flow were evident between NRDL in the CFD simulations (Fig. 6). The magnitude and intensity of these jets varied with time and were most prominent at peak systole.

We also observed the formation of vortical structures in the CFD results during flow reversal (see Animation#3 in supplementary materials (Supplemental videos are available under the "Supplemental Data" tab for this paper on the ASME Digital Collection)). These structures were not detected in the 4D PCMRI results, since they were only present during CSF flow reversal, when CSF velocities were small compared to the velocity encoding (VENC) value used for the 4D PCMRI sequence. In addition, the CFD results showed synchronous bidirectional CSF flow. This was due to the m-shaped Womersley profile that occurred during CSF flow reversal; an observation that has been reported in previous CFD studies of CSF flow around the spinal cord [17–19,26,27].

Discussion

Improvement in our understanding of CSF dynamics has the potential to aid assessment and treatment options for pathologies of the CNS such as CMI. To date, there have been a limited number of systematic comparisons of PCMRI measurements and CFD simulations for quantification of CSF flow parameters. Recent application of 4D PCMRI to CSF flows has enabled quantification of CSF velocity in 3D space and time [11,12,21]. As such, the comparison between 4D PCMRI and 3D subject-specific CFD simulations can help to gain a deeper understanding of their potential for evaluation of CSF dynamics in health and disease.

This study provides the first subject-specific comparison of CSF velocity fields in the cervical SSS using 4D PCMRI and CFD simulations that includes NRDL. A previous subject-specific CFD study by our group without NRDL showed large CSF flow differences in comparison to 4D PCMRI measurements [21]. Thus, our approach was to perform a variational analysis to determine if the use of a more anatomically accurate CFD model, including idealized NRDLs, resulted in a more favorable comparison to in vivo 4D PCMRI measurements. We compared the 4D PCMRI and CFD CSF flow field under two different hydrodynamic conditions by including a single healthy subject and CMI patient in the study.

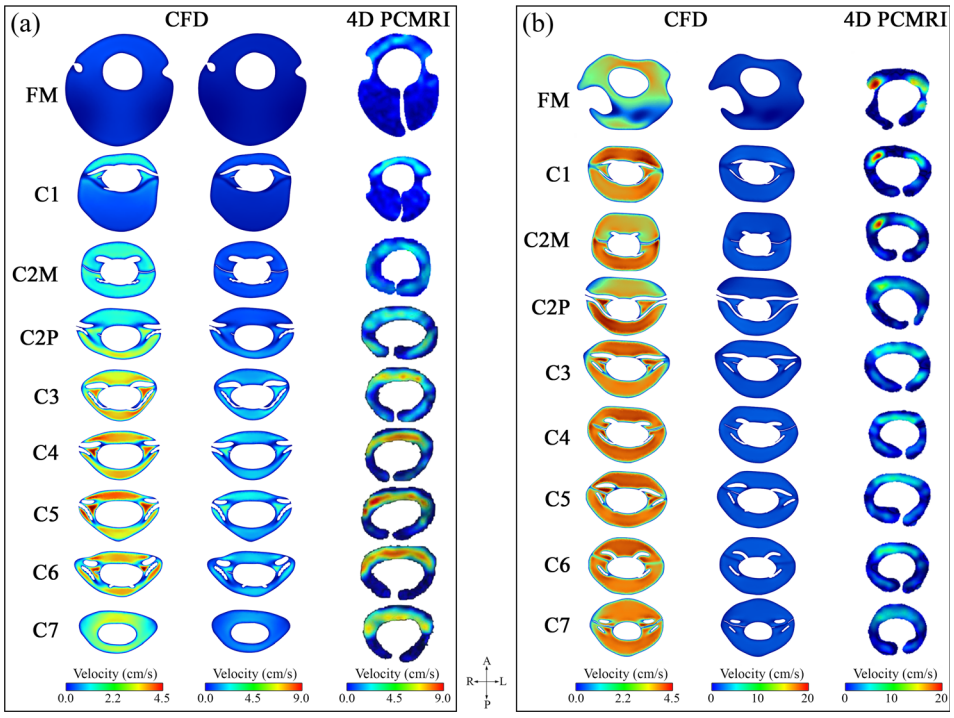

Fig. 4 Distribution of through-plane peak systolic velocity magnitude at different locations along the cervical spine plotted (*a*) for the healthy case and (*b*) for the CMI patient. In each set of contours, the left and right column represents the results obtained from the CFD simulation and 4D PCMRI measurements, respectively. Note: CFD results are shown in two columns; one with a velocity range identical to 4D PCMRI and another with a smaller velocity range to show detail in the CFD velocity profiles.

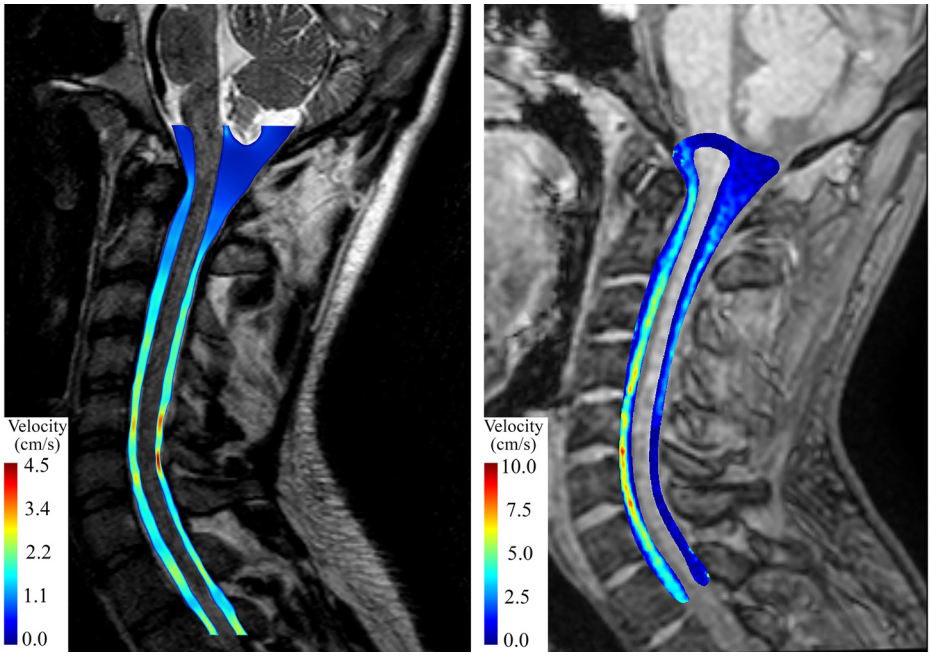

Fig. 5 Distribution of midsagittal peak systolic velocity magnitude for the healthy subject obtained from CFD (left) and 4D PCMRI (right). Note that the magnitude images used to obtain the CFD geometry (left) had higher resolution than those obtained by 4D PCMRI (right).

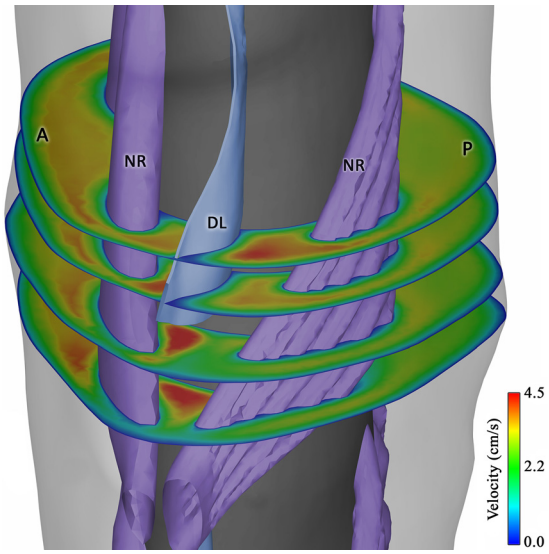

Fig. 6 Formation of concentrated velocity regions (jets) between nerve rootlets (NR) and denticulate ligaments (DL). The anterior and posterior side of the geometry is represented by "A" and "P," respectively. Note that due to the variable insertion lines of the idealized DLs into the spinal cord, these structures were not completely extended inferiorly between the rootlets at some levels, such as the depicted level.

Differences in Peak CSF Velocities. CSF velocities were consistently greater for the 4D PCMRI measurements obtained in the cervical spine compared to the CFD simulations. The discrepancy between the CFD and 4D PCMRI peak systolic velocities varied widely depending on the axial level. The greatest differences between in vivo and CFD velocities was present at regions with high CSF velocities such as the lower cervical planes (C3–C7) in the healthy case and upper cervical planes (FM–C2P) in the CMI patient (Fig. 3). In regions where NRDL were not present, CFD velocity profiles were relatively blunt compared to 4D PCMRI for a given axial location (Fig. 4). The heterogeneities of peak velocity distribution observed in the present study 4D PCMRI results were similar to those reported in many in vivo studies [1,8–10,12,21].

The 4D PCMRI values of peak systolic and diastolic velocities ranged from 1.4 to 5.6× greater than CFD for the healthy and CMI patient (Fig. 3). This discrepancy was more pronounced in the CMI patient at the FM where 4D PCMRI peak systolic velocities were more than 5× greater than CFD. The CFD-simulated CSF velocities obtained in the present study were maximized by choosing the subject-specific CSF flow boundary condition based on the axial level along the spine with the greatest CSF flow waveform amplitude (Fig. 2). However, even with these CSF flow boundary conditions, the resulting peak CFD velocities were much smaller than the 4D PCMRI measurements for the patient and healthy models. A greater discrepancy in CFD and 4D PCMRI measurements is expected if the CSF flow boundary conditions were based on any other axial level with a smaller waveform amplitude.

Results from this study and a previous study by our group [21] both show large discrepancy between velocities obtained by CFD and 4D PCMRI (up to eightfold difference). However, better agreement between CFD simulations and PCMRI velocities have been reported [26,28,29]. Cheng et al. [26] measured velocity waveforms at one point at C2 for a healthy subject and reported lower values of systolic and diastolic velocities measured by 2D PCMRI compared to a subject-specific CFD simulation. Clarke et al. [29] analyzed CSF velocity waveforms from 2D PCMRI measured at ten monitoring locations at C2 and C5 for one healthy and two CMI patients. At C2, the velocity waveforms compared more favorably than at C5. At C5, the 2D PCMRI measurements showed low CSF velocities on the posterior side of the spinal cord compared to the anterior side; a similar feature observed in the present study. At this location the posterior 2D PCMRI measurements of peak CSF velocities obtained by Clarke et al. were up to ~5× smaller than the CSF velocities that were simulated by CFD.

The different comparison techniques (e.g., comparison of velocity distribution at axial planes versus comparison of velocities at monitoring points/regions) and CFD modeling boundary conditions used in the current and previous studies make it

difficult to directly compare results. The present study and others by our group [21] are the first to compare 4D PCMRI and CFD of CSF flow in the cervical spine. The cited studies used 2D PCMRI for comparison to CFD and found better agreement. Future studies with detailed comparison/validation of CFD simulation results and in vivo 2D and 4D PCMRI measurements of CSF flow are needed.

Similarities in Velocity Distribution. CSF velocity distributions obtained from CFD simulations and 4D PCMRI measurements had some similarities. Anterior and anterolateral dominance of flow was observed in the 4D PCMRI measurements and CFD simulations (Fig. 4). Similar flow features have been reported in vivo [7,8,10–12,21]. A previous numerical study demonstrated that it is likely that this flow pattern is present only when NRDL are added to the CFD model [19]. The anterior and anterolateral CSF flow dominance occurred at peak CSF flow, as also observed in vivo [12,30]. These CSF flow features were not observed in previous CFD studies without NRDL [17,18,21]. This dominance was less pronounced in the CFD compared to in vivo which suggests the importance of other factors such as heterogeneous resistance against CSF flow in SSS as discussed in the "Sources of Error" section.

Lateral regions with elevated CSF velocity (jets) between dorsal and ventral NRDLs were another flow feature observed in the CFD simulations (Figs. 4 and 6). These jets were present to a greater degree in the lower cervical SSS and more noticeable in the healthy case (C4 to C6). Evidence of these bilateral concentrated regions of CSF flow in the lower cervical spine was detected at some of the 4D PCMRI axial planes (Fig. 4) and in a previous 4D PCMRI study completed by our group [21]. These jets have not been observed in CFD simulations without NRDLs.

Sources of Error

The differences between velocity patterns seen in vivo by 4D PCMRI measurements and by CFD modeling are difficult to reconcile, as the 4D PCMRI technique has not been extensively validated for CSF flow measurements and thus cannot be considered a gold standard for comparison. The following factors are thought to be likely sources for the observed differences:

(1) lack of the heterogeneous resistance against CSF flow in the CFD model
(2) lack of neural tissue motion in the CFD geometry
(3) lack of tissue compliance in the CFD model
(4) anatomic accuracy of the CFD model
(5) PCMRI VENC value and signal to noise
(6) ROI truncation near the edges of the 4D PCMRI flow field

CFD Modeling Sources of Error

Lack of the Heterogeneous Resistance Against CSF Flow in the CFD Model. The presence of fine anatomical structures, such as arachnoid trabeculae, was not considered in the current CFD model; we believe this to be a major factor leading to the velocity differences. The large differences in anterior versus posterior CSF flow velocities observed in the 4D PCMRI measurements, but not in the CFD simulations, could be due to uneven distribution of arachnoid trabeculae and the presence of midline septations of the arachnoid membrane that were not included in the CFD geometry. Studies in the literature have shown heterogeneous distribution of arachnoid trabeculae with higher density in the posterior and upper cervical SSS in dogs [31]. The presence of midline dorsal and dorsolateral septa and the absence of arachnoid condensations or septations along the ventral SSS have been reported in cadaveric observations [32,33]. Under this condition, resistance against CSF flow is expected to be lower in the anterior SSS and thus, CSF velocities in this region would be greater. More detailed in vivo quantification of the fine structures inside the SSS would allow implementation of a more accurate CFD model.

Lack of Neural Tissue Motion in the CFD Geometry. The motion of neural tissues could be an important factor leading to the observed differences in CFD and 4D PCMRI results, in particular, near the FM for the patient case. Several studies have quantified bulk motion of neural tissues. Oldfield et al. [34] reported abrupt downward movement of the cerebellar tonsils in CMI patients during decompression surgery using intraoperative ultrasound. Oscillatory motion of the cervical spinal cord and cerebellar tonsils has been found to be ~1 mm in the craniocaudal direction in healthy subjects and CMI patients [35,36]. Greater bulk motion of the spinal cord and cerebellar tonsils in CMI patients versus healthy controls [36] and CMI patients with and without syringomyelia [37] has been reported. Milhorat et al. [38] and Bunck et al. [12] reported pronounced alterations in CSF flow and peak velocities in CMI patients associated with increased motion of the cerebellar tonsils for patients with relatively mild morphological alterations. Bunck et al. [12] reported that elevated CSF velocities at the craniocervical junction in CMI patients were accompanied by increased brain stem motion. Similarly, Yiallourou et al. [21] suggested that the structural motion of the cerebellar tonsils and the resulting reduction in the cross-sectional area of the upper SSS may alter CSF velocities near the FM.

We hypothesize that the motion of the cerebellar tonsils, brain stem, and spinal cord resulted in elevated CSF velocities near the FM in the patient case and that our CFD simulation had lower velocities due to a lack of neural tissue motion. NRDL are difficult to identify by T2-weighted MR images acquired at 3T. It is possible that the NRDLs move to a small degree over the cardiac cycle due to the CSF pulsation and motion of the spinal cord. If present, the structural motion could result in blurred appearance of the NRDLs on time-averaged T2 MRI measurements. Simulations and MRI measurements could be conducted to understand the role of neural tissue motion and its impact on CSF velocities near the FM and along the spinal cord.

Lack of Tissue Compliance in the CFD Model. Compliance of the SSS may have led to significant differences in the CSF velocity results. Compliance of the SSS is evident by the CSF flow amplitude change that was observed along the spine from the FM to the first thoracic vertebrae (Fig. 2). Similar alterations in CSF flow amplitude have been documented by our group in another CSF flow study conducted at multiple axial levels along the spine [21]. Evidence of SSS compliance was also documented by MRI quantification of CSF velocity wave speed in the SSS [39]. Cheng et al. [40] showed that the interaction of CSF and surrounding tissues can impact CSF velocities to a great degree. More studies are needed to better quantify the elastic properties of neural tissues and to implement those properties in CFD models.

Anatomic Accuracy of the CFD Model. The CFD model of spinal cord and dura mater geometry was subject-specific, but the NRDLs were idealized based on ex vivo anatomical measurements in the literature. This was a requirement because these structures are not reliably detectable on a subject-specific basis using MRI. Also, a single operator segmented both subject-specific geometries of the cervical SSS. Although we do not expect these anatomical inaccuracies to be a factor leading to the large difference between the 4D PCMRI and CFD velocities, further studies should be performed to assess the use of high-resolution 7T MRI [41] to segment SSS geometries with subject-specific NRDL. In addition, possible interoperator variability of the segmented geometry, the possible impact of contrast enhancement, and/or other factors that may bias the segmented surfaces should be evaluated.

A constant pressure boundary condition was imposed at the cranial end of the CFD geometries due to the difficulty in obtaining pressure in vivo at this location. Due to the complexity of the geometry at the upper cervical SSS, a uniform pressure outflow could alter velocity distributions in this region. Future simulations

with more extended geometries that include the cisterns in the craniovertebral junction could lead to more accurate results.

4D PCMRI Sources of Error. A detailed review of sources of error for 4D PCMRI is provided by Elkins and Alley [42]. Herein, we describe some of the key factors leading to error in the present study.

PCMRI VENC Value and Signal to Noise Ratio (SNR). In PCMRI, the VENC value is adjusted to avoid phase wrapping artifacts (aliasing) while also maintaining a SNR in a reasonable range for flow within the entire region of interest. The VENC choice can be difficult when peak velocities vary to a great degree within the region of interest. For the present study, the VENC was chosen based on the maximum CSF velocity anticipated throughout the cervical SSS in each subject. Thus, the 4D PCMRI sensitivity was reduced within regions with low CSF velocities relative to the VENC (e.g., FM and C1 in the healthy model). At these regions, CSF flow rate may have been underestimated.

In 4D PCMRI measurements, SNR is linearly related to voxel volume and can be increased by choosing lager voxels [42]. However, the increase in voxel size will result in lower spatial resolution and can decrease the ability of 4D PCMRI measurements to distinguish complex flow features. SNR is also proportional to the square root of the length of time over which measurements are obtained and it can be improved by increasing the acquisition time [42]. The 4D PCMRI sequence used in the present study was designed for clinical use (∼10 min total acquisition time). Obtaining 4D PCMRI under higher spatial–temporal resolution data with a longer time acquisition would be helpful to understand how these factors can impact the in vivo velocity results.

ROI Truncation Near the Edges of the 4D PCMRI Flow Field. A difference in the CFD model and 4D PCMRI measurement slice areas was visible at many locations along the cervical spine (see ROI differences in Fig. 4). These differences were present because the CFD geometries were created based on the segmentation of high-resolution T2 MRI images and not based on the lower resolution PCMRI magnitude images. In addition, the presence of noise in the 4D PCMRI scan required significant truncation of the cross-sectional slices near the flow edges and thus resulted in smaller ROIs relative to the CFD models. We do not expect peak PCMRI velocities to be impacted by truncation of slices near the walls, where CSF velocities were nearly zero. However, truncation of the 4D PCMRI cross-sectional areas may have led to underestimation of the CSF flow that was used for the CFD simulation, although this is expected to have a relatively small impact on CFD velocities.

Limitations

A single healthy subject and CMI patient were selected for the study. The healthy subject was considerably older than the patient and thus likely to have different flow characteristics [8]. The intent of this study was not to determine differences between the patient and healthy case, but rather compare the 4D PCMRI and CFD simulations within each case to better understand their potential in evaluating CSF dynamics. As such, the differences in CSF dynamics measured by 4D PCMRI and CFD within each model remain relevant to the aim of the study.

The axial variation of CSF flow measured by 4D PCMRI (Fig. 2) was not accounted for in the rigid-wall CFD models used in the present study. Fluid structure interaction or moving boundary modeling of the cervical spine could help account for the measured axial variation of CSF flow.

The relatively small number of time points in 4D PCMRI technique used in the present study resulted in temporal averaging of the in vivo CSF velocities within the specified phases and thus lower peak CSF velocities than reality. We expect that measurement of CSF velocities with a higher temporal resolution 4D PCMRI sequence would result in an even greater discrepancy between the CFD and 4D PCMRI results.

Bulk motion of the body over the cardiac cycle could alter the CSF flow. This possible component of CSF flow was excluded from the CFD model used in the current study, since our CSF flow assessment technique did not take into account any bulk motion of the body and/or neural tissues.

Conclusion

Comparison of in vivo 4D PCMRI measurements and subject-specific 3D CFD simulations, including idealized NRDL, showed considerably different CSF flow features and velocity magnitudes. 4D PCMRI showed 1.4–5.6× greater peak CSF velocities than CFD with the greatest differences present in the CMI patient near the cerebellar tonsils. Future studies are needed to understand the differences observed between CFD and 4D PCMRI results by investigating the sources of error for 4D PCMRI measurements and CFD simulation of CSF flow in the SSS.

Acknowledgment

The authors acknowledge Conquer Chiari, National Institutes of Health (NINDS) Grant No. 1R15NS071455-01 and the Swiss National Science Foundation Grant No. 205321_132695/1 for support of this work. The authors also thank Gerard Crelier from GyroTools LLC for support with the visualization and analysis of the 4D PCMRI data presented in this study.

References

[1] Bunck, A. C., Kroeger, J. R., Juettner, A., Brentrup, A., Fiedler, B., Crelier, G. R., Martin, B. A., Heindel, W., Maintz, D., Schwindt, W., and Niederstadt, T., 2012, "Magnetic Resonance 4D Flow Analysis of Cerebrospinal Fluid Dynamics in Chiari I Malformation With and Without Syringomyelia," Eur. Radiol., **22**(9), pp. 1860–1870.

[2] Clarke, E. C., Stoodley, M. A., and Bilston, L. E., 2013, "Changes in Temporal Flow Characteristics of CSF in Chiari Malformation Type I With and Without Syringomyelia: Implications for Theory of Syrinx Development," J. Neurosurg., **118**(5), pp. 1135–1140.

[3] Martin, B. A., Labuda, R., Royston, T. J., Oshinski, J. N., Iskandar, B., and Loth, F., 2010, "Spinal Subarachnoid Space Pressure Measurements in an In Vitro Spinal Stenosis Model: Implications on Syringomyelia Theories," ASME J. Biomech. Eng., **132**(11), p. 111007.

[4] Bradley, W. G., Jr., Scalzo, D., Queralt, J., Nitz, W. N., Atkinson, D. J., and Wong, P., 1996, "Normal-Pressure Hydrocephalus: Evaluation With Cerebrospinal Fluid Flow Measurements at MR Imaging," Radiology, **198**(2), pp. 523–529.

[5] Hsu, Y., Hettiarachchi, H. D., Zhu, D. C., and Linninger, A. A., 2012, "The Frequency and Magnitude of Cerebrospinal Fluid Pulsations Influence Intrathecal Drug Distribution: Key Factors for Interpatient Variability," Anesth. Analg., **115**(4), pp. 879–879.

[6] Papisov, M. I., Belov, V. V., and Gannon, K. S., 2013, "Physiology of the Intrathecal Bolus: The Leptomeningeal Route for Macromolecule and Particle Delivery to CNS," Mol. Pharm., **10**(5), pp. 1522–1532.

[7] Haughton, V. M., Korosec, F. R., Medow, J. E., Dolar, M. T., and Iskandar, B. J., 2003, "Peak Systolic and Diastolic CSF Velocity in the Foramen Magnum in Adult Patients With Chiari I Malformations and in Normal Control Participants," AJNR. Am. J. Neuroradiol., **24**(2), pp. 169–176.

[8] Iskandar, B. J., Quigley, M., and Haughton, V. M., 2004, "Foramen Magnum Cerebrospinal Fluid Flow Characteristics in Children With Chiari I Malformation Before and After Craniocervical Decompression," J. Neurosurg., **101**(2 Suppl), pp. 169–178.

[9] Quigley, M. F., Iskandar, B., Quigley, M. E., Nicosia, M., and Haughton, V., 2004, "Cerebrospinal Fluid Flow in Foramen Magnum: Temporal and Spatial Patterns at MR Imaging in Volunteers and in Patients With Chiari I Malformation," Radiology, **232**(1), pp. 229–236.

[10] Krueger, K. D., Haughton, V. M., and Hetzel, S., 2010, "Peak CSF Velocities in Patients With Symptomatic and Asymptomatic Chiari I Malformation," AJNR. Am. J. Neuroradiol., **31**(10), pp. 1837–1841.

[11] Bunck, A., Kroeger, J., Juettner, A., Brentrup, A., Fiedler, B., Crelier, G., Martin, B., Heindel, W., Maintz, D., Schwindt, W., and Niederstadt, T., 2012, "Magnetic Resonance 4D Flow Analysis of Cerebrospinal Fluid Dynamics in Chiari I Malformation With and Without Syringomyelia," Eur. Radiol., **22**(9), pp. 1860–1870.

[12] Bunck, A. C., Kroger, J. R., Juttner, A., Brentrup, A., Fiedler, B., Schaarschmidt, F., Crelier, G. R., Schwindt, W., Heindel, W., Niederstadt, T., and Maintz, D., 2011, "Magnetic Resonance 4D Flow Characteristics of Cerebrospinal Fluid at the Craniocervical Junction and the Cervical Spinal Canal," Eur. Radiol., **21**(8), pp. 1788–1796.

[13] Santini, F., Wetzel, S. G., Bock, J., Markl, M., and Scheffler, K., 2009, "Time-Resolved Three-Dimensional (3D) Phase-Contrast (PC) Balanced Steady-State Free Precession (BSSFP)," Magn. Reson. Med., **62**(4), pp. 966–974.
[14] Sweetman, B., and Linninger, A. A., 2011, "Cerebrospinal Fluid Flow Dynamics in the Central Nervous System," Ann. Biomed. Eng., **39**(1), pp. 484–496.
[15] Matsumae, M., Hirayama, A., Atsumi, H., Yatsushiro, S., and Kuroda, K., 2013, "Velocity and Pressure Gradients of Cerebrospinal Fluid Assessed With Magnetic Resonance Imaging," J. Neurosurg., **120**(1), pp. 218–227.
[16] Stadlbauer, A., Salomonowitz, E., Brenneis, C., Ungersbock, K., van der Riet, W., Buchfelder, M., and Ganslandt, O., 2012, "Magnetic Resonance Velocity Mapping of 3D Cerebrospinal Fluid Flow Dynamics in Hydrocephalus: Preliminary Results," Eur. Radiol., **22**(1), pp. 232–242.
[17] Linge, S. O., Haughton, V., Lovgren, A. E., Mardal, K. A., Helgeland, A., and Langtangen, H. P., 2011, "Effect of Tonsillar Herniation on Cyclic CSF Flow Studied With Computational Flow Analysis," AJNR. Am. J. Neuroradiol., **32**(8), pp. 1474–1481.
[18] Linge, S. O., Haughton, V., Lovgren, A. E., Mardal, K. A., and Langtangen, H. P., 2010, "CSF Flow Dynamics at the Craniovertebral Junction Studied With an Idealized Model of the Subarachnoid Space and Computational Flow Analysis," AJNR. Am. J. Neuroradiol., **31**(1), pp. 185–192.
[19] Heidari Pahlavian, S., Yiallourou, T., Tubbs, R. S., Bunck, A. C., Loth, F., Goodin, M., Raisee, M., and Martin, B. A., 2014, "The Impact of Spinal Cord Nerve Roots and Denticulate Ligaments on Cerebrospinal Fluid Dynamics in the Cervical Spine," PLoS ONE, **9**(4), p. e91888.
[20] Shaffer, N., Martin, B., and Loth, F., 2011, "Cerebrospinal Fluid Hydrodynamics in Type I Chiari Malformation," Neurol. Res., **33**(3), pp. 247–260.
[21] Yiallourou, T. I., Kröger, J. R., Stergiopulos, N., Maintz, D., Martin, B. A., and Bunck, A. C., 2012, "Comparison of 4D Phase-Contrast MRI Flow Measurements to Computational Fluid Dynamics Simulations of Cerebrospinal Fluid Motion in the Cervical Spine," PLoS ONE, **7**(12), p. e52284.
[22] Alleyne, C. H., Jr., Cawley, C. M., Barrow, D. L., and Bonner, G. D., 1998, "Microsurgical Anatomy of the Dorsal Cervical Nerve Roots and the Cervical Dorsal Root Ganglion/Ventral Root Complexes," Surg. Neurol., **50**(3), pp. 213–218.
[23] Lang, J., 1993, *Clinical Anatomy of the Cervical Spine*, G. Thieme Verlag, University of Wurzburg, Germany.
[24] Tubbs, R. S., Salter, G., Grabb, P. A., and Oakes, W. J., 2001, "The Denticulate Ligament: Anatomy and Functional Significance," J. Neurosurg., **94**(2 Suppl), pp. 271–275.
[25] Bloomfield, I. G., Johnston, I. H., and Bilston, L. E., 1998, "Effects of Proteins, Blood Cells and Glucose on the Viscosity of Cerebrospinal Fluid," Pediatr. Neurosurg, **28**(5), pp. 246–251.
[26] Cheng, S., Stoodley, M. A., Wong, J., Hemley, S., Fletcher, D. F., and Bilston, L. E., 2012, "The Presence of Arachnoiditis Affects the Characteristics of CSF Flow in the Spinal Subarachnoid Space: A Modelling Study," J. Biomech., **45**(7), pp. 1186–1191.
[27] Loth, F., Yardimci, M. A., and Alperin, N., 2001, "Hydrodynamic Modeling of Cerebrospinal Fluid Motion Within the Spinal Cavity," ASME J. Biomech. Eng., **123**(1), pp. 71–79.
[28] Rutkowska, G., Haughton, V., Linge, S., and Mardal, K. A., 2012, "Patient-Specific 3D Simulation of Cyclic CSF Flow at the Craniocervical Region," AJNR. Am. J. Neuroradiol., **33**(9), pp. 1756–1762.
[29] Clarke, E. C., Fletcher, D. F., Stoodley, M. A., and Bilston, L. E., 2013, "Computational Fluid Dynamics Modelling of Cerebrospinal Fluid Pressure in Chiari Malformation and Syringomyelia," J. Biomech., **46**(11), pp. 1801–1809.
[30] Bunck, A. C., Kroeger, J. R., Juettner, A., Brentrup, A., Fiedler, B., Crelier, G. R., Martin, B. A., Heindel, W., Maintz, D., Schwindt, W., and Niederstadt, T., 2012, "Magnetic Resonance 4D Flow Analysis of Cerebrospinal Fluid Dynamics in Chiari I Malformation With and Without Syringomyelia," Eur. Radiol., **22**(9), pp. 1860–1870.
[31] Malloy, J. J., and Low, F. N., 1976, "Scanning Electron Microscopy of the Subarachnoid Space in the Dog. IV. Subarachnoid Macrophages," J. Comp. Neurol., **167**(3), pp. 257–283.
[32] Key, E., and Retzius, M., 1876, *Studien in der Anatomie des Nervensystems und des Bindegewebes*, Samson & Wallin, Stockholm, Sweden.
[33] Nauta, H. J., Dolan, E., and Yasargil, M. G., 1983, "Microsurgical Anatomy of Spinal Subarachnoid Space," Surg. Neurol., **19**(5), pp. 431–437.
[34] Oldfield, E. H., Muraszko, K., Shawker, T. H., and Patronas, N. J., 1994, "Pathophysiology of Syringomyelia Associated With Chiari I Malformation of the Cerebellar Tonsils. Implications for Diagnosis and Treatment," J. Neurosurg., **80**(1), pp. 3–15.
[35] Mikulis, D. J., Wood, M. L., Zerdoner, O. A., and Poncelet, B. P., 1994, "Oscillatory Motion of the Normal Cervical Spinal Cord," Radiology, **192**(1), pp. 117–121.
[36] Cousins, J., and Haughton, V., 2009, "Motion of the Cerebellar Tonsils in the Foramen Magnum During the Cardiac Cycle," AJNR. Am. J. Neuroradiol., **30**(8), pp. 1587–1588.
[37] Hofmann, E., Warmuth-Metz, M., Bendszus, M., and Solymosi, L., 2000, "Phase-Contrast MR Imaging of the Cervical CSF and Spinal Cord: Volumetric Motion Analysis in Patients With Chiari I Malformation," AJNR. Am. J. Neuroradiol., **21**(1), pp. 151–158.
[38] Milhorat, T. H., Chou, M. W., Trinidad, E. M., Kula, R. W., Mandell, M., Wolpert, C., and Speer, M. C., 1999, "Chiari I Malformation Redefined: Clinical and Radiographic Findings for 364 Symptomatic Patients," Neurosurgery, **44**(5), pp. 1005–1017.
[39] Kalata, W., Martin, B. A., Oshinski, J. N., Jerosch-Herold, M., Royston, T. J., and Loth, F., 2009, "MR Measurement of Cerebrospinal Fluid Velocity Wave Speed in the Spinal Canal," IEEE Trans. Biomed. Eng., **56**(6), pp. 1765–1768.
[40] Cheng, S., Fletcher, D., Hemley, S., Stoodley, M., and Bilston, L., 2014, "Effects of Fluid Structure Interaction in a Three Dimensional Model of the Spinal Subarachnoid Space," J. Biomech., **47**(11), pp. 2826–2830.
[41] Sigmund, E. E., Suero, G. A., Hu, C., McGorty, K., Sodickson, D. K., Wiggins, G. C., and Helpern, J. A., 2012, "High-Resolution Human Cervical Spinal Cord Imaging at 7 T," NMR Biomed., **25**(7), pp. 891–899.
[42] Elkins, C. J., and Alley, M. T., 2007, "Magnetic Resonance Velocimetry: Applications of Magnetic Resonance Imaging in the Measurement of Fluid Motion," Exp. Fluids, **43**(6), pp. 823–858.